Supplement of Aerosol Research, 3, 477–502, 2025 https://doi.org/10.5194/ar-3-477-2025-supplement © Author(s) 2025. CC BY 4.0 License.





Supplement of

AIDA Arctic transport experiment – Part 1: Simulation of northward transport and aging effect on fundamental black carbon properties

Marco Zanatta et al.

Correspondence to: Marco Zanatta (m.zanatta@isac.cnr.it) and Gholam Ali Hoshyaripour (gholamali.hoshyaripour@kit.edu)

The copyright of individual parts of the supplement might differ from the article licence.

Supplementary

5

S1. Correction of SP2 detection limit

100 x10⁻³ Measured size distribution (53-362 nm) mass size distribution [-] Lognormally fitted size distribution (10-1000 nm) Estimated mass loss below detection limit (<53 nm) 80 60 40 20 ż 5 6 7 100 10 1000 rBC particle diameter [nm]

Figure S 1 Example of mass size distribution and lognormal fit to estimate the mass concentration of rBC particles below the detection limit of the SP2. Dots: mass size distribution as measured by the SP2, organized in 50 bins covering the 51-370 nm diameter range. Green line: lognormal curve fitted to the measured mass size distribution. Yellow area: estimated mass below the 51 nm, used to correct the rBC mass concentration of the SP2. The example represents the first hours of summer low altitude experiment.

5 S2. Latitudinal profiles of atmospheric conditions

Table S1 Latitudinal profiles of irradiation time, temperature and relative humidity (ERA5), and NO2/BC ratio (CAMS) for the ARCTEx transport scenarios: summer low-altitude (SL), summer high-altitude (SH), winter low-altitude (WL), winter high-altitude (WH). Latitudinal profiles extracted in the region of interest between 40°N and 90°N, in the pressure range 1000-800 hPa (low-altitude) and 600-400 hPa (high-altitude), in July (summer) and January (Winter). 40-90°N transport corresponding to 5 experimental days in AIDA (10°N = 1 experimental day). Median calculated for equidistant latitude bands 10° wide.

Experiment day	1	2	3	4	5
Simulated latitude [°N]	40-50	50-60	60-70	70-80	80-90
Irradiation time [h]					
SL – SH	16	20	22	24	24
WL - WH	8	4	2	0	0
Temperature [°C]					
SL	21	15	11	3.0	0.0
SH	-35	-39	-40	-40	-41
WL	-9.0	-16	-21	-21	-21
WH	-52	-55	-57	-57	-58
Relative humidity [%]					
SL	55	69	68	78	83
SH	47	56	55	49	48
WL	63	78	86	85	85
WH	44	57	62	61	60

NO ₂ /BC ratio [-]					
SL	2.8	0.78	0.60	0.22	0.20
SH	4.2	2.4	1.6	1.5	1.39
WL	6.7	11	9.6	3.9	1.6
WH	8.2	10	12	10	7.5

25

Table S2 Daily mean of experimental conditions measured in the AIDA chamber for the ARCTEx transport scenarios: summer low-altitude (SL), summer high-altitude (SH), winter low-altitude (WL), winter high-altitude (WH). 40-90 $^{\circ}$ N transport corresponding to 5 experimental days in AIDA (10° N = 1 experimental day). Median calculated for equidistant latitude bands 10° wide.

Experiment day	1	2	3	4	5
Simulated latitude [°N]	40-50	50-60	60-70	70-80	80-90
Irradiation time [h]					
SL - SH	16	20	22	24	24
WL -WH	8	4	2	0	0
Temperature, T [°C]					
SL	21	15	10	3	0.0
SH	-35	-40	-41	-41	-41
WL	-9.8	-16	-20	-21	-22
WH	-52	-56	-58	-59	-59
Relative humidity, RH					
[%]					
SL	44	62	65	77	79
SH	53	63	58	49	49
WL	57	72	75	74	71
WH	56	57	57	57	58
NO ₂ /BC ratio [-]					
SL	3.5	2.0	2.0	2.8	5.2
SH	2.8	1.7	1.0	1.3	1.6
WL	5.4	7.6	6.4	2.2	3.3
WH	5.7	6.8	12	8.2	7.5

30

Table S3 Ratio between daily averaged AIDA conditions over latitudinally averaged ERA5 and CAMS data.

Experiment day	1	2	3	4	5
Simulated Latitude [°N]	40-50	50-60	60-70	70-80	80-90
Measured/simulated ratio					
Temperature [-]					
SL	1.00	1.00	0.99	1.00	1.00
SH	1.00	0.99	0.99	0.99	0.99
WL	0.99	1.00	1.00	0.99	0.99
WH	0.99	0.99	0.99	0.99	0.99
Relative humidity [-]					
SL	0.80	0.90	0.96	1.00	0.95
SH	1.13	1.12	1.06	1.01	1.03
WL	0.90	0.93	0.89	0.87	0.85
WH	1.27	1.01	0.92	0.94	0.97
NO2/BC ratio [-]					
SL	1.25	2.53	3.37	12.87	26.10
SH	0.65	0.69	0.68	0.86	1.15
WL	0.81	0.66	0.67	0.55	2.13
WH	0.70	0.66	1.07	0.82	1.00

35 S3. Characterization of fresh mini-CAST soot

In this section, we describe the fundamental properties of fresh soot injected in the AIDA chamber, aged in dark conditions and in the absence of ozone and nitrogen dioxide for less than 60 minutes after the injection time (Table 1) under the 4 transport scenario conditions.

The number size distribution measured with the SMPS showed a non-negligible variability characterized by a minimum geometric mean diameter of 80 nm for SL to a maximum of 104 nm for SH, while the winter experiments shared a relatively similar size of around 92-93 nm (Figure S 2a). Although these values were similar to previous studies measuring soot produced with diffusion flame burners with slightly different oxidative air flows (Ess et al., 2021; Maricq, 2014; Moore et al., 2014; Rissler et al., 2013), we expected higher reproducibility of BC mobility diameter. Part of this variability may be explained by differences in injection duration, as longer injections tend to favor rapid coagulation, leading to larger particle sizes. The soot showed a clear decrease of effective density with particle diameter (Figure S 2b), as expected for fractal aggregates. During the low-altitude experiments, the density showed a common decrease of ρ_e from 400 kg m⁻³ at 100 nm to 200 kg m⁻³ at 250 nm, being in agreement with diffusion-flame soot (Ess et al., 2021; Rissler et al., 2013). However, these ARTCEx values were substantially lower compared to mini-CAST soot obtained under different combustion regimes (Ess et al., 2021; Moore et al., 2014; Yon et al., 2015) and to BC standards such as fullerene soot and acquadag (Gysel et al., 2011). Interestingly, the soot injected at colder temperatures (WH and SH) was denser, with $\rho_{\rm e}$ ranging from 590-770 kg m⁻³ at 100 nm to 220-380 kg m⁻³ at 250 nm. Similar to density, the soot injected in AIDA showed lower fractal dimensions compared to previous studies (Figure S 2c). Low $d_{\rm f}$ values (2.01-2.21) indicated the production of complex aggregates, agreeing with the low effective density discussed above. As a matter of fact, diesel soot (Olfert et al., 2007), and diffusion (Rissler et al., 2013) or premix (Cross et al., 2010) soot was characterized by already more compact aggregates. The rBC mass fraction (F_{rBC}) was compared with EC/TC fractions observed in previous studies. The latter showed high variabilities connected with the type of fuel (diesel, EC/TC=0.6, Liu et al., 2018) and 60 combustion conditions (diffusion and premixed flame; Ess et al., 2021). During all ARCTEx experiments, the fraction of rBC appeared to decrease with the particle diameter from a maximum of 95% to a minimum of 75%. This range fell between the premixed McKenna burner (Cross et al., 2010) and the diffusion mini-CAST burner with oxidative air flows of 1.60-1.55 (Ess et al., 2021; Schnaiter et al., 2006). The comparison between F_{rBC} and EC/TC ratio must be treated with caution, given the systematic differences observed between the mass concentration of rBC and EC (Pileci et al., 2021). The low density and diameter values observed in SH and WH suggest that the lower injection temperatures (-35 to -52 °C) compared to the warmer temperatures in SL and WL (25 to -9 °C)may have promoted early condensation of semi-volatile compounds on the soot cores, leading to compaction of the originally ramified structure. However, the fractal dimension and rBC mass fraction did not fully confirm this hypothesis. Despite the slightly higher density and lower fractal dimension, the soot particles produced during

be partially responsible for the difference observed in the low-altitude and high-altitude scenarios.

Although the fraction of coating apparently did not change, cold temperature might already cause a partial collapse of the ramified structure, leading to smaller, already denser fresh soot particles.

ARCTEx appeared to be representative of soot generated with various diffusion burners operated at similar flow rates of propane and oxidative air. It is interesting to note that the injection temperature might

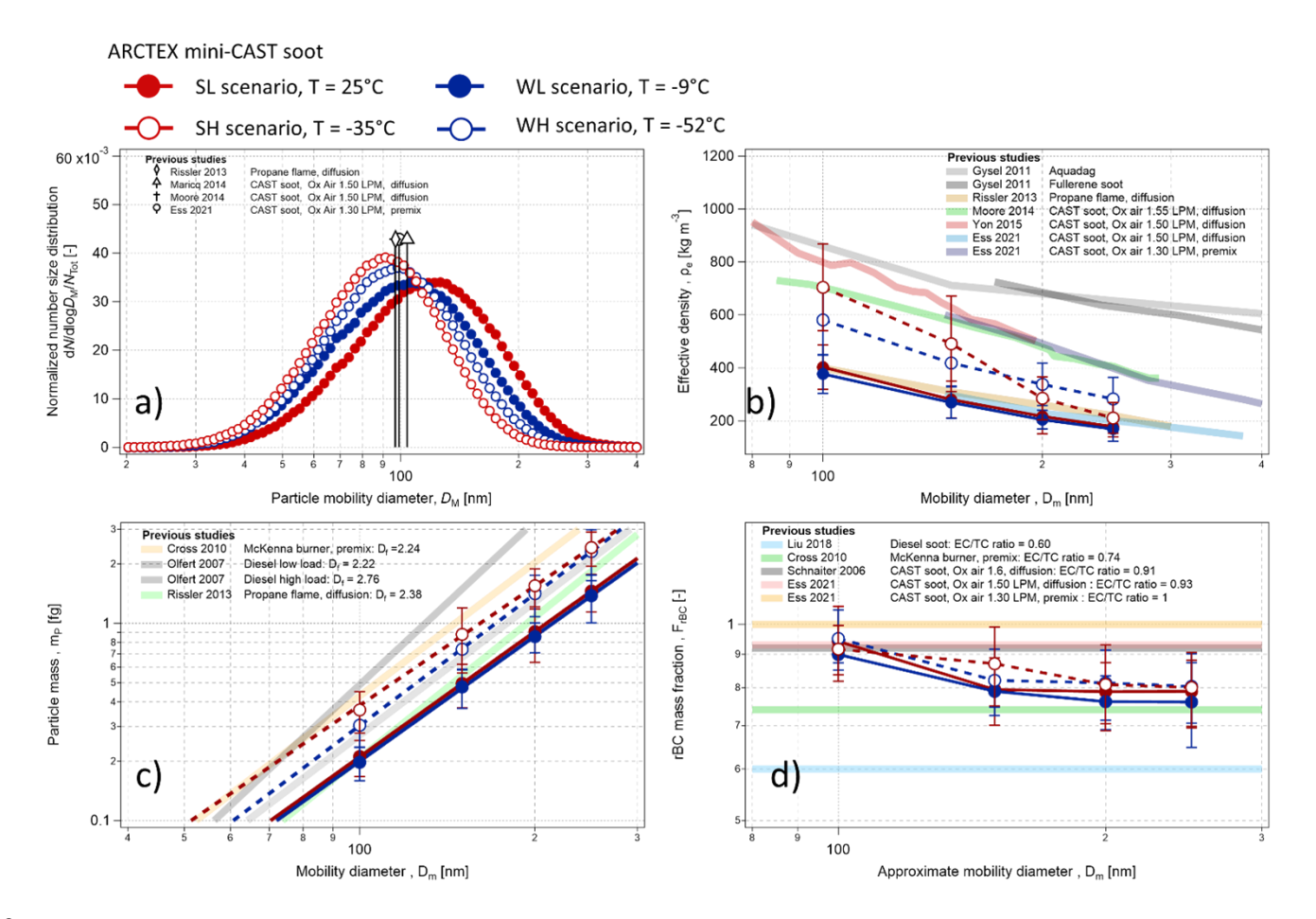


Figure S 2 Characterization of fresh soot before aging (absence of oxidants and light) during the various transport scenarios in AIDA: a) number size distribution measured with a scanning mobility particle sizer; b) effective density and diameter relationship measured with the combined setup of a differential mobility analyzer and an aerosol particle mass analyzer; c) mass and diameter relationship measured with the combined setup of a differential mobility analyzer and an aerosol particle mass analyzer; d) rBC mass fraction and diameter relationship the combined setup of a differential mobility analyzer, an aerosol particle mass analyzer and a single particle soot photometer. Soot produced with the mini-CAST burner (series 5200) operated with 60 μLPM of propane, 1.55 LPM of oxidation air, 7.5 LPM of N₂ and 13 LPM of dilution air. Scenarios: summer low-altitude (SL), winter low-altitude (WL), summer high-altitude (SH) and winter high-altitude (WH).

S4. Mass concentration closure

90

By combining the DMA-APM-SP2 scans (Section 2.4.4 and Section 2.4.5) with the online and independent measurements performed by the SMPS and SP2 we performed a mass closure of the of the total aerosol mass present inside the AIDA chamber volume.

The M_{rBC} measured by the SP2 was converted into the mass concentration of the total aerosol (M_{p-SP2}) by means of the particle-by-particle coating mass fraction as:

$$M_{p-SP2} = M_{rBC} \left(1 + \frac{Fm_{coat}}{Fm_{rBC}} \right)$$
 S1

Here we assumed that the particle-by-particle mass fraction of rBC and coating is representative of the rBC population, requiring a homogeneous coating degree across the SP2 detection size range.

The number size distribution of total particles measured by the SMPS was converted into a mass size distribution by accounting for the size-dependent effective density to determine the corresponding particle mass concentration (M_{p-SMPS}):

$$M_{p-SMPS} = \sum_{D_0}^{D_{max}} N_{Di-SMPS} * \rho_e(D_{i-SMPS}) * \frac{\pi D_{i-SMPS}^3}{6}$$
 S2

where $\rho_e(D_{\text{i-SMPS}})$ is the effective density at a specific diameter of the SMPS size distribution ($D_{\text{i-SMPS}}$) and $N_{\text{i-SMPS}}$ its number concentration.

 $\rho_{\rm e}(D_{\rm i-SMPS})$ was extrapolated as a function of the mass-to-diameter relationship, which is described by an exponential function with the exponent ($d_{\rm f}$) and constant ($k_{\rm f}$) as follows:

$$\rho_e(D_{i-SMPS}) = \frac{6}{\pi} \frac{m_{Di-SMPS}}{D_{Di-SMPS}^3} = \frac{6}{\pi} \frac{\left(k_f * D_{i-SMPS}\right)^{df}}{(D_{i-SMPS})^3}$$
 S3

The $M_{p\text{-}SP2}$ was compared with the $M_{p\text{-}SMPS}$ to evaluate the accuracy of the independent measurement techniques, including DMA-APM, DMA-APM-SP2, SMPS, SP2, and AMS. This comparison also aimed to assess the validity of various assumptions, such as the material densities of BC, organic matter, and nitrate. The comparison was based on simultaneous measurements from the SP2 and SMPS, conducted one hour before and after each DMA-APM-SP2 scan.

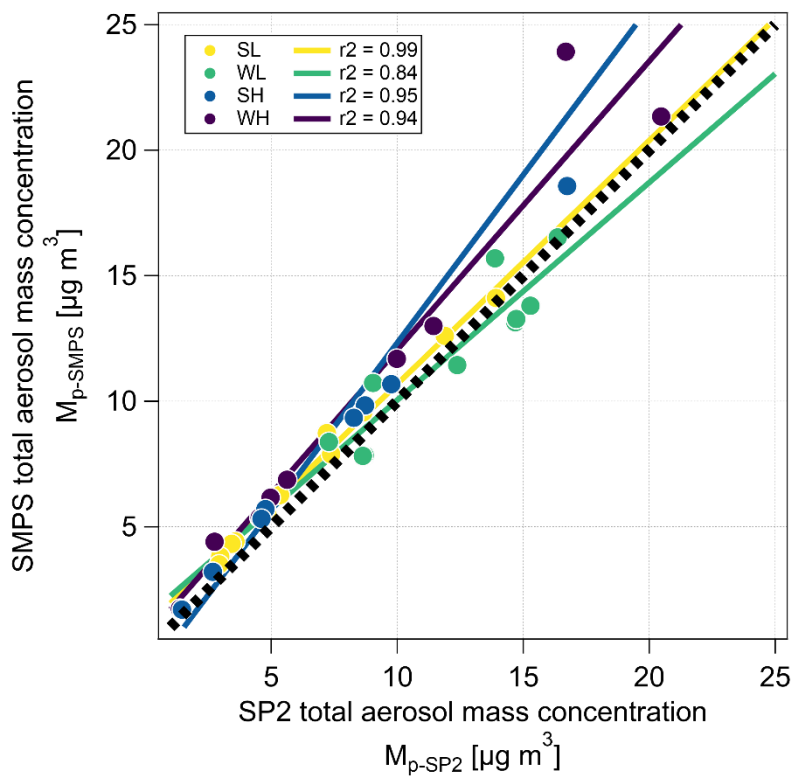


Figure S 3 Scatter plot with linear fitting between the total aerosol mass concentration derived from the SMPS and SP2.

S5. Characterization of diameter evolution

115

120

We investigated the temporal evolution of the geometric mean of the number size distribution of rBC (D_{NrBC-GM}) measured with the SP2, its growth factor (GF_{DrBC}, calculated as the ratio of D_{rBC-GM} at t_x to D_{rBC-GM} before t₀) and its growth rate (GR_{DrBC}, calculated as change of D_{NrBC-GM} in a period Δt normalized over the period duration). The evolution of GF_{DrBC} and GR_{DrBC} is shown in Figure S4a. Since rBC particles in the chamber are the refractory component and are assumed to be spherical in SP2 calculations, changes in D_{NrBC-GM} are attributed solely to intra-coagulation growth. Coagulation rates increases with particle concentration (more collisions at higher concentrations) and the coagulation kernel, which varies with particle diameter and diffusion coefficient (Naumann, 2003). In high-altitude experiments, fast

coagulation rates in the first 4 hours (GR_{DrBC} > 2 nm h⁻¹) caused a 50% diameter increase within 24 hours (50°N) and 85% by the experiment's end (90°N). In SL, lower rBC concentrations led to slower growth $(GR_{DrBC} \approx 1.5 \text{ nm h}^{-1})$, resulting in a 38% diameter increase within 24 hours (50°N) and 65% by the end 135 (90°N). Despite the different growth rate, diameter increased in these three experiments following an exponential curve. GF_{DrBC} deviated from exponential growth in WL after the second aging step (t_{24}), when GR_{DrBC} dropped to 0.1 nm h⁻¹ while effective density, fractal dimension, and coating mass fraction increased (50°N; Figure 5). Despite the higher concentration compared to SL, rBC particles showed the slowest growth in WL, with final GF_{DrBC} below 60% (90°N). As discussed in Section 3.3, the higher 140 number and mass concentration in AIDA compared to ambient conditions might enhance coagulation and diameter growth. In WL, the diameter growth deviated from exponential function to a linear function in WL after the second aging step (t₂₄), when fractal dimension, and coating mass fraction increased (50°N; Figure 5). Particle restructuring at the onset of coating may have reduced the active surface area, thereby limiting the collision frequency and coagulation rate. This hypothesis aligns with numerical simulations 145 of Naumann (2003), suggesting that coating formation may reduce coagulation rates near the sources or in polluted regions. Although particle coagulation has been extensively studied in other settings (Schnaiter et al., 2003; Maricq, 2007), our finding rises the need of targeted experiments to quantify the change of coagulation rate of soot particles in the transition regime from external to internal mixing in ambient like conditions.

In a second analysis step, we investigated the temporal evolution of the geometric mean of the number size distribution of total particles ($D_{Np\text{-}GM}$) measured with the SMPS, its growth factor (GF_{Dp} , calculated as the ratio of $D_{Np\text{-}GM}$ at t_x to $D_{Np\text{-}GM}$ before t_0) and its growth rate (GR_{Dp} , calculated as change of $D_{Np\text{-}GM}$ in a period Δt normalized over the period duration). The evolution of GF_{Dp} and GR_{Dp} is shown in Figure S4b.

155 Whereas coagulation increases diameter while maintaining external mixing (Naumann, 2003), coating deposition first compacts and reduces size (Schnaiter et al., 2003; Yuan et al., 2020), then increases diameter with coating thickening (Li et al., 2017). These processes occurred across different ARCTEx scenarios. Exponential growth by coagulation was only observed during the coldest experiment (WH), when no internal mixing was observed. The slight increase of ρ_e (Figure 5a) may have caused a deviation 160 from exponential growth in SL, when the slow GR_{Dp} decreased at t₂₄, indicating a weaker coagulation growth. Although rapid growth occurred in the first 24 hours (50°N) of SL, GF_{Dp} decreased by 6% within 4 hours after the second aging step (t₂₄), indicating BC compaction similar to Schnaiter et al. (2003). The steady increase in density and coating (Figure 5) caused the gradual collapse of BC 's ramified structure, leading to a reduction in GF_{Dp} from 61% at t₂₄ to 53% at t₇₂ and a negative GR_{Dp}. After 70°N, as particles 165 approached spherical shapes, coating thickening drove growth, resulting in a final GF_{Dp} of 80% (90°N). Thin organic coatings (Fm_{coat} ≈ 0.20) can compact fractal BC, reducing its mobility diameter (Bambha et al., 2013). In WL, no exponential growth occurred. Rapid compaction likely took place in the very first moment of the first aging step, followed by efficient nitrate deposition, which increased the coating thickness of near-spherical particles in a stepwise manner, with growth rates exceeding 2 nm h⁻¹. Coating 170 growth appeared to be particularly efficient in the first 72 hours (70°N), when GF_{Dp} reached 90% and slowed afterwards. A similar step-wise growth was observed during medium-duration aging experiments

Overall, Figure S4b indicates that intra-coagulation may lead to faster growth then condensation and coating formation. Nevertheless, even thin coatings may influence particle growth on short time scale (WL and SL) and long-time scale (SH).

in AIDA (Schnaiter et al., 2005).

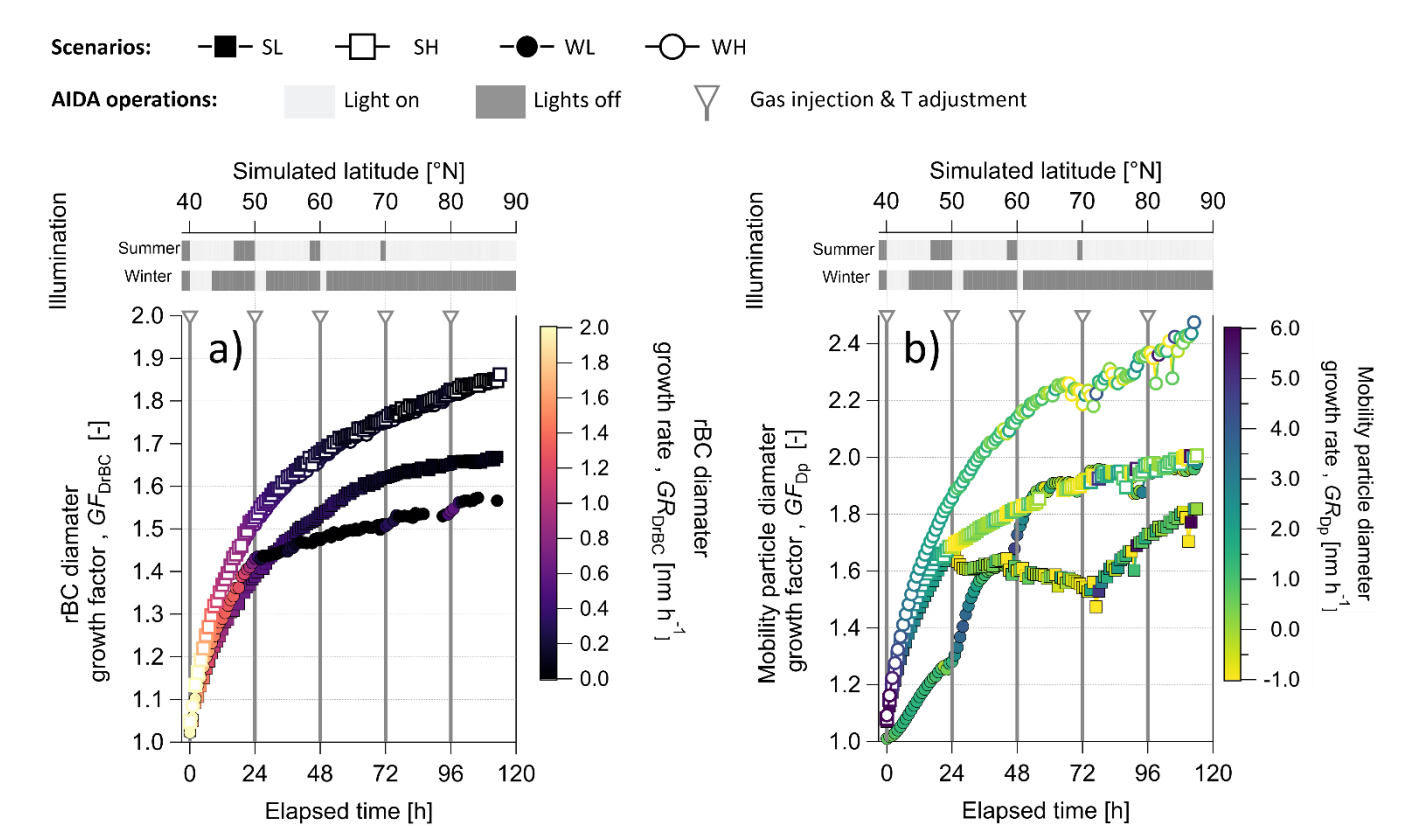


Figure S4 Temporal and latitudinal evolution of the growth factor and growth rate for: a) rBC particles measured with the SP2; b) total particles measured with the SMPS. ARCTEx scenarios: summer low-altitude (SL), winter low-altitude (WL), summer high-altitude (SH), winter high-altitude (WH).